Multi-length Scale Morphology of Nonfullerene All-Small Molecule Blends and Its Relation to Device Function in Organic Solar Cells

Research Article

Multi-length Scale Morphology of Nonfullerene All-Small Molecule Blends and Its Relation to Device Function in Organic Solar Cells

Indunil Angunawela[1], Long Ye[1], Haijun Bin[2], Zhi-Guo Zhang[2], Abay Gadisa[1], Yongfang Li[2*] and Harald Ade[1*]*

[1]Department of Physics and Organic and Carbon Electronics Lab (ORaCEL), North Carolina State University, Raleigh, NC 27695, United States

E-mail: hwade@ncsu.edu; lye4@ncsu.edu

[2]CAS Research/Education Center for Excellence in Molecular Sciences, CAS Key Laboratory of Organic Solids, Institute of Chemistry, Chinese Academy of Sciences, 100190 Beijing, China

E-mail: liyf@iccas.ac.cn

Keywords: nonfullerene organic solar cell; all-small molecule blends; multi-length morphology; composition variation; side chain effect

Abstract

Nonfullerene all-small molecule organic solar cells (OSCs) have attracted significant attention due to their competitive performance compared to the well-studied polymer-based OSCs. Small molecules are considered to be materials of choice for industrial scale OSC production due to their relatively high purity, reproducibility, and well-defined molecular weights. Despite the recent progress in all-small molecule solar cells, the mesoscale morphology of these devices remains elusive. A fundamental understanding of the structure-property relationships of these systems is thus critical for further device performance enhancement. Here, we report a dramatic

change in device performance of a nonfullerene all-small molecule bulk heterojunction system upon changing the side chains of the electron donor small molecules. Morphology analysis via resonant soft X-ray scattering shows that the average composition variation and the size of the smaller domains of the all-small molecule blends are the most influential factors that derive the photogeneration and collection efficiency of charges in efficient all-small molecule OSCs. The observed side-chain and processing initiated morphological changes resulted in distinct device efficiencies in these systems. Despite the fact that side chains are mainly meant to facilitate materials dissolution, the current study clearly shows that they can also impose an immense effect on material organization and photovoltaic properties. The findings will give a clear understanding of the role of side chains and processing on material organization and device functionality, and the knowledge gained in this study is quite crucial in designing next-generation materials and devices.

1. Introduction

Unlike traditional inorganic solar cells, organic solar cells (OSCs) offer several unique features that enable integration of this technology with infrastructures, vehicles and many other applications. This driving force has led to the synthesis of various electron donor and acceptor materials that have recently led to record-breaking OSCs.[1, 2] The success of OSCs is highly influenced by the type of the donor/acceptor bulk heterojunction blend utilized as a photoactive layer. In particular, recent performance breakthroughs were made because of replacing the benchmark fullerene molecules with non-fullerene small molecule electron acceptors (NFAs) that strongly convert red photons to electricity in addition to transporting free electrons.[3-5] Following this line, the research of OSCs has also focused on utilizing an all-small molecule

active layer by getting rid of polymer donors as well mainly due to the fact that small molecules can relatively be well purified, reproduced, and have well-defined molecular weights.[6-8] Recent efforts have led to highly efficient nonfullerene all-small molecule OSCs whose performance is gradually approaching that of devices utilizing polymer electron donors.[9-19] The most critical factors in OSC fabrication is not only designing the right materials or choosing the right combination of materials but also optimizing the device parameters by controlling the morphology of the active layers to optimize photocurrent production and transport.[20-26] However, while the morphology of the polymer/acceptor blends has relatively been well studied and optimized, the fundamentals of the structure-property relationships at mesoscale is still poorly understood for the nonfullerene all-small molecule systems[19, 27].

In both polymer and small molecule donors, benzodithiophene (BDT) unit has been very popular over the past years due to its enhanced electron delocalization and low highest occupied molecular orbital energy (HOMO) level.[7, 28-30] Following the high efficiency shown by two-dimensional conjugated D-A copolymers based on bithienylbenzodithiophene (BDTT) and fluorobenzotriazole (FBTA) as donor and acceptor, respectively, Bin *et al*. synthesized a high-performance A-D-A structured organic molecule H11[31] using BDTT as the donor unit and FBTA as the acceptor unit with ethylhexyl cyanoacetate unit as the end group to improve the electron affinity. As it has been shown for different polymers, having conjugated side groups in the BDT unit leads to a significant change in device performance.[29] A control molecule H12[31] with alkoxy instead of alkylthienyl conjugated side chain was synthesized to investigate the effect of side chain on solar cell performance (**Figure 1**) in small molecule donor systems. H11 with conjugated side chain shows better absorption, low-lying HOMO energy level, better carrier mobility and bimodal crystallites in blends with IDIC compared to H12 which are favorable for

device performance. The H11:IDIC blend has demonstrated a remarkable PCE of 9.73%, which was among the highest reported values for all-small molecule OSCs. Although the current efficiency has surpassed this limit, as shown in **Figure 1** due to the similarity of the backbone with BDTT, H11 seems to be a good and representative model system for an in-depth morphological study.

Resonant soft X-ray scattering (R-SoXS)[32] is an advanced tool that can be used to quantify average composition variation and size of the domains and helped the OSC community to build new morphology-performance relationships in a large number of polymer-based OSCs. Although grazing incidence wide-angle X-ray scattering has been used to explain the observed difference in device performance of all-small molecule nonfullerene OSCs as a function of chemical structure[11, 14, 27, 31], a clear resonant soft X-ray scattering (R-SoXS) study, which has become a standard to investigate the length scale of phase separation in organic photovoltaic research, is rarely performed in this field of research. Here, we discuss the quantitative morphology-performance relations for a pair of all-small molecule systems based on representative small molecule H11 and its analog H12, without conjugated side chains. In composite organic semiconductor films, charge generation and transport are directly influenced by the morphology of the photoactive film, and this eventually affects device performance. The change from alkoxy to conjugated side chain (alkylthienyl) in the donor molecule has shown a significant difference in the performance. Therefore, an investigation on morphology-performance relationships will definitely be necessary for further development of the all-small molecule nonfullerene OSCs and its side chain engineering.
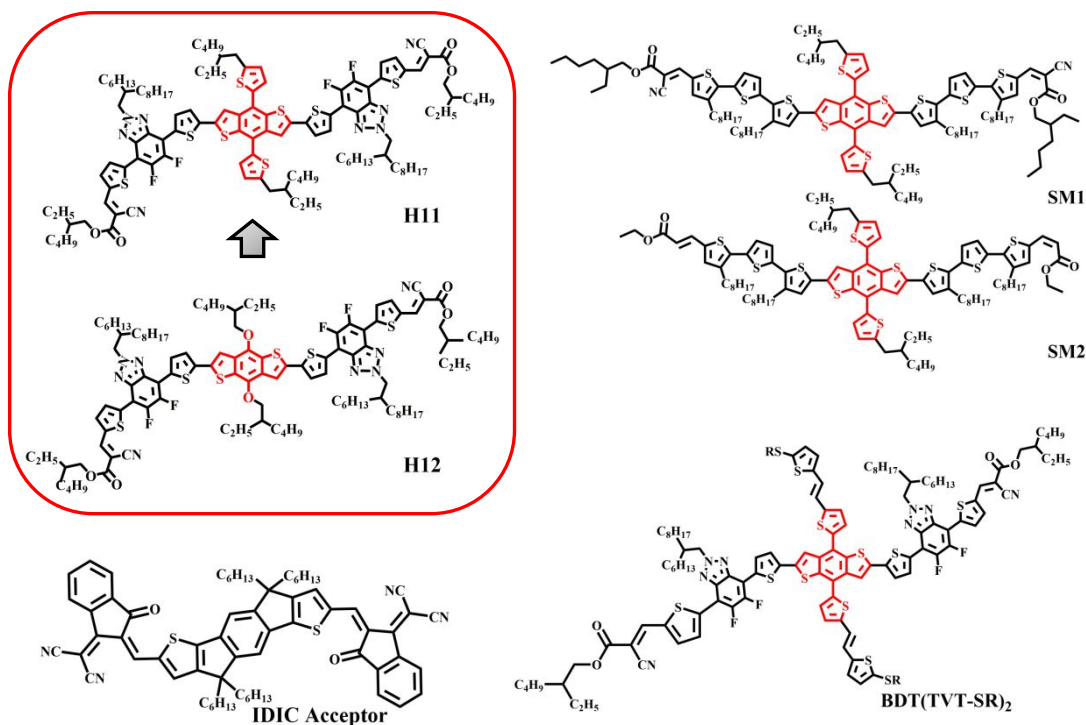
Figure 1. H11, H12 small molecules (top left) used in the study and some of the small molecule donors based on central BDT unit with thienyl substitution together with the common non-fullerene acceptor IDIC used in the nonfullerene all-small molecule OSCs.

2. Experimental Methods

Samples for measurements and the active layer of the devices were prepared using the same conditions as those used for device fabrication.[31] The active layers were spin coated from a chloroform solution with 2:1 weight ratio of donor:acceptor inside a N_2 glove box. The annealed active layers were thermally annealed at 120 ^{0}C for 10 minutes.

2.1 R-SoXS measurements

R-SoXS measurements were performed in transmission geometry with linearly polarized photons under high vacuum (1×10^{-7} Torr) at beamline 11.0.1.2[33, 34] at the Advanced Light Source (ALS). The scattering 2D images were collected in-vacuum cooled 2D charge-coupled

device (CCD) detector (Princeton Instruments, PI-MTE, 2048 × 2048 pixels). The soft X-ray energies were tuned between 270 and 285 eV in the RSoXS experiments. Using a custom Nika[35] analysis package, 2D scattering patterns were reduced to 1D scattering profiles and normalized for the X-ray flux. Since distance traveled through the samples by the X-rays affect the scattering intensity, it was normalized for absorption and film thicknesses. Samples for R-SoXS measurements were first prepared on a polystyrene sulfonate (PSS) modified Si substrate and floating in water to a 1.5×1.5 mm, 100 nm thick Si3N4 membrane supported by a 5×5 mm, 200 μm thick Si frame.

2.2 Photoluminescence measurements.

Steady-state photoluminescence spectra were obtained with a FL/FS920 from Edinburgh Instruments, equipped with an excitation source of 450 W xenon arc lamp. In all cases, long pass sorting filters were utilized to remove unwanted higher energy light that passes through the excitation monochromator. To probe blends, an excitation wavelength of 685 nm was used. In order to normalize for the thickness, the obtained spectra were normalized with the absorption at the excitation wavelength.

2.3 Device characterization.

The *J-V* characterization was performed inside a nitrogen-filled glove box with a computer-controlled Keithley 2400 source meter, whiles the samples were exposed to a white light of 100 mW/cm^2 intensity generated by an AM 1.5G solar simulator (Oriel Sol3A, Newport Corporation) that was calibrated to 1 Sun with a NREL certified KG-5 filtered silicon reference diode. PAIOS system (Fluxim) was used to perform the light intensity dependent photovoltaic measurements.

3. Results and Discussion

The morphology of all-small molecule bulk heterojunction blend was thoroughly investigated using a synchrotron radiation-based technique, RSoXS. The mesoscale properties of the molecular scale domains will be discussed in detail. Furthermore, inverted all-small molecule solar cells were fabricated and characterized and their outputs are correlated with morphological properties. Overall, the results help to investigthe the detailed morphology-function relationship, a key element that is needed for material and device optimization.

3.1 Multi-length scale morphology

RSoXS aids in realizing the variation in the average composition which is directly related to device properties. Therefore, R-SoXS serves as a complementary technique to grazing-incidence wide-angle X-ray scattering to get a complete morphological picture at the mesoscale and to build morphology-device performance relationships.

It is noted that improper miscibility of the materials in the blend is one of the major factors that adversely affect device performance of all-small molecule OSC, and this morphological factor is highly controlled by the donor-acceptor intermolecular interactions[36, 37]; highly miscible molecules lead to the formation of too impure domains while low miscibility leads to large and over-purified domains hindering the charge dissociation process. In the current report, this challenge question is investigated by tuning the interactions between the molecules in the blend through side chain engineering and device processing. To explore the phase separation at different length scales and to assess the role of morphology on device performance, R-SoXS experiment was performed at the beamline 11.0.1.2 at the Advanced Light Source (ALS).
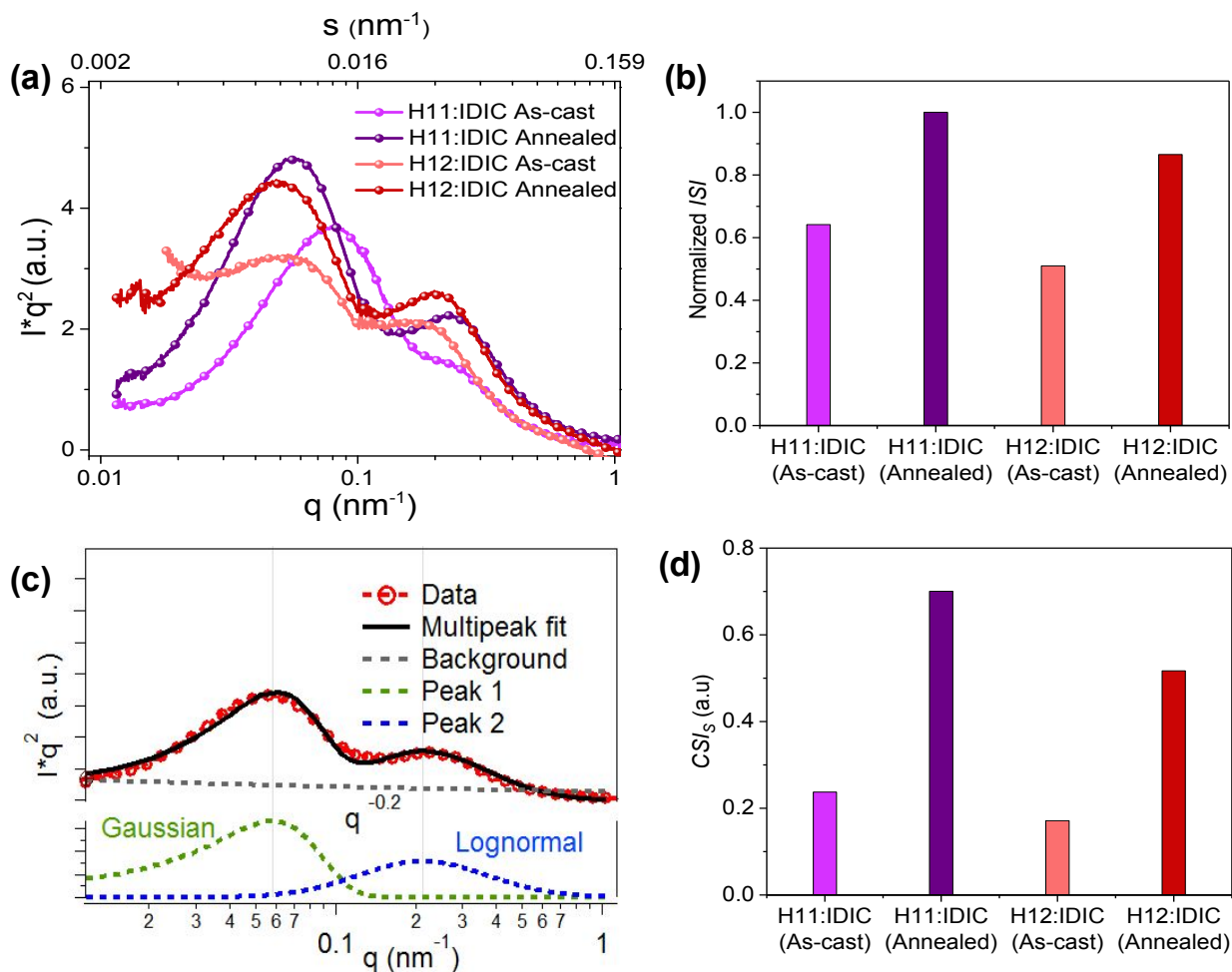
Figure 2 (a) Thickness/absorption normalized and Lorentz corrected R-SoXS profiles obtained at 283.6 eV. s is the spatial frequency, which can be transformed into momentum transfer with $q=2\pi s$. (b) Plot of ISI for various blend films. ISI normalized to the annealed H11:IDIC sample at 283.6 eV. (c) Multi-peak fit for the R-SoXS profile of the annealed H11:IDIC sample at 283.6 eV. A log-normal and a Gaussian peak are required to obtain a good fit. (d) Component scattering intensity (CSI_S) of high q domains for each blend at 283.6 eV.

In RSoXS measurements, differences in the material refractive index are used to distinguish between materials[38], and the average composition variation is proportional to the square root of integrated scattering intensity. Completely mixed domains provide a negligible signal. According

to our previously established protocols[32], the integrated scattering intensity (*ISI*) of organic blend films can be used to quantify the relative domain purity, which was found to be a mostly linear relation with device fill factor. Long period is often correlated with the short-circuit current (J_{sc}).

Table 1 The long period, total *ISI*, and *CSI* values for each peak at 283.6 eV.

Sample	Long Period (nm)		Normalized ISI	CSI	
	Low q peak	High q peak		Low q peak	High q peak
H11:IDIC (As-cast)	83	34	0.64	0.26	0.37
H11:IDIC (Annealed)	108	29	1	0.3	0.7
H12:IDIC (As-cast)	152	38	0.51	0.18	0.34
H12:IDIC (Annealed)	132	34	0.86	0.26	0.6

RSoXS profiles were acquired **(Figure 2a)** near the absorption edge where high material contrast is achieved and Lorentz corrected[39]. All the energies ranging from 283 eV to 284.2 eV show consistent results **(Figure S1)** with dual peak fitting, one lognormal peak at high q and a Gaussian peak at low q **(Figure 2c)** to achieve good fits. This bimodal size distribution with two well-defined peaks is related to phase separation at two different length scales. This has been observed in all polymer OSC system[40]. Lognormal peak, in general, occurs in nature[41] when a number of factors are contributing to phase separation while a Gaussian peak is attributable to control over a single variable[40]. **Figures 2b,** and **d** show the normalized integrated scattering intensity (*ISI*) and the component scattering intensity (*CSI*)[42] of the high q domains for each blend, both as-cast and annealed. The corresponding scattering intensity of each peak component is obtained by integrating the scattering intensitiesthe of fitted profile. In multiphase systems, the square root of CSI is proportional to the domain purity of the particular domain. Normalized *ISI* and *CSI* in the H11 system are greater than those of the H12 system for both the as-cast and

annealed blends. The long period values of both domains, normalized ISI, and CSI values of the

two domains for all the samples are summarized in **Table 1**.

To confirm these morphological differences further in terms of domain purity,

photoluminescence (PL) quenching studies were performed. The samples were prepared with the

same processing conditions and the data obtained is normalized to material absorption at the

excitation wavelength to eliminate the influence of film thickness. PL flux significantly increases

with annealing compared to the as-cast blend **(Figure S3)**. As a supplement to the reciprocal

method, power spectral densities (PSD)[43] of the AFM phase images **(Figure S4)**, via the Fourier

transform analysis was done to check the multi-length scale morphology of the blends. It

confirms the existence of two domain sizes and the long periods of the domains also agrees well

with the values obtained from R-SoXS, which is around 0.15 nm^{-1} for high-q peak and 0.03 nm^{-1}

for the low-q peak. The AFM height image also shows the multi-length scale morphology which

confirms that the bulk and surface morphology are very similar.

3.2 Charge Extraction and Recombination

Excellent carrier generation and extraction efficiencies are crucial for achieving high

efficiency in operational solar cells. These highly material-type and blend structure dependent

processes need to be assessed and understood properly to develop materials and device designs

that enable the development of highly efficient OSCs. Here, to gain insight into the charge

carrier generation dynamics of the all-small molecule solar cells, inverted devices with

ITO/ZnO/donor: acceptor (2:1, w/w)/MoO_3/Al structure were fabricated with and characterized

(See Table S1). To probe charge generation dynamics, the photogenerated current (J_{ph}) was

measured by varying the device internal voltage ($V_0 = V_{applied} - V_{built-in}$). J_{ph} is estimated by

subtracting the current measured in the dark from that measured under the light. **Figure 3a** shows the J_{ph} measured under illumination of one Sun light intensity for both H11 and H12 based annealed devices. The J_{ph}-V_0 curves are characterized with varying slopes depending on the magnitude of V_0. At very low effective voltage (<0.2 V), J_{ph} shows a linear dependence on voltage, while a square-root dependence is observed in V_0 range of 0.2-0.8 V originating from unbalanced electron and hole mobilities.[44] The photocurrent saturates for a voltage range exceeding 0.8 V, and in this specific region the photocurrent is expressed as $J_{ph}= eGL$[44, 45], where e is the electric charge, G is the generation rate and L is the active layer thickness. The generation rate at the saturation region is 1.23×10^{27} m^{-3}s^{-1}, and 8.26×10^{26} m^{-3}s^{-1} for the optimized H11 and H12 solar cells, respectively. Despite the similarities in backbone structure, these two materials have clearly resulted in a substantially different photocurrent yield in solar cells.

For further analysis of charge dynamics, the J_{ph} of the solar cells was measured at different light intensities and effective voltages (**Figure S2**). In this case, J_{ph} is expected to have a power law dependence on light intensity P_{light} and should follow $J_{ph} \propto P_{light}^{\alpha}$, where the exponent α may refer to charge collection or loss rates. Inferring to **Figure 3b**, which shows α as a function of effective voltage, it can be seen that α assumes unity in the region corresponding to the saturation regime depicted in **Figure 3a**, while its value drops dramatically near the open-circuit voltage (lower V_0) indicating a strong bimolecular recombination in this region.[46, 47]
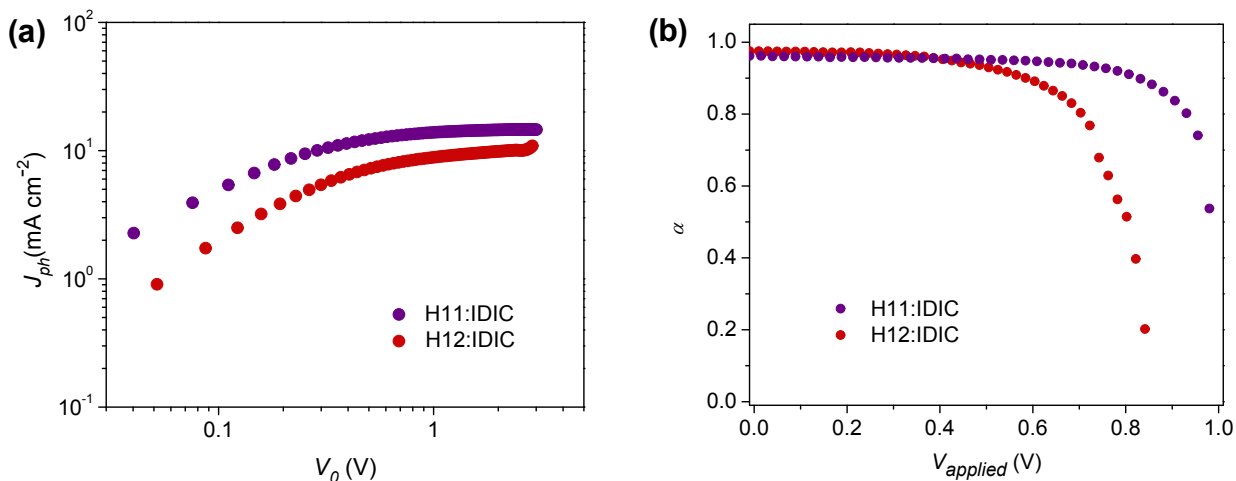
Figure 3 (a) Photocurrent (J_{ph}) vs effective applied voltage V_0 at 1 Sun for annealed OSC devices; (b) α as a function of the voltage applied to the annealed OSC devices.

It is also shown that α deviates from unity near open circuit voltage (V_{oc}) more severely for the H12 system (**Figure S5**) than the H11-based devices, indicating the former devices subjected to more losses. The ideality factor for each system was also obtained at different light intensities (**Figure S6**). For devices measured under one Sun illumination, the ideality factor was calculated to be 0.95 for the H11-based annealed solar cells indicating that losses at open-circuit voltage are mostly bimolecular in nature. Corresponding H12-based devices are identified with an ideality factor of 1.49, which signals a strong effect of traps near the open-circuit voltage. The charge carrier generation and loss analyzed in this section will further be discussed in light of the observed morphological behaviors in the following section.

3.3 Fundamental connections and Implications

The clear difference in morphology of the two systems has clearly contributed to the photovoltaic properties. This section is dedicated to connecting the morphology-performance correlations to fully understand the role of side chain structure on device performance. In both

the systems, device parameters (*FF* and J_{sc}) increases upon annealing. *FF* increases from 49.5% to 65.4% in H11-based system and from 38.2% to 54.9% in H12 based system. J_{sc} also shows a similar trend by increasing from 10.99 mA cm^{-2} to 15.21 mA cm^{-2} and from 4.94 mA cm^{-2} to 10.51 mA cm^{-2} for H11 and H12-based systems respectively in the conventional structure devices.[31]The device performance parameters of inverted devices were provided in **Table 2**. It is clear that inverted and regular device configurations give consistent trends. According to the R-SoXS results summarized in **Table 1**, *ISI* is increased upon annealing of each sample, which is indicative of domains getting purer[48] and the long period of the smaller domains decreased over annealing which helps better charge dissociation. Therefore, the post-processing has optimized the phase seperation betewen the donor and the acceptor in these all small molecule systems, which is mostly the case in bulk-heterojunction solar cells. The size and purity of the nanoscale domains are important parameters in the charge generation and collection processes of OSCs. In the current study, we observed a clear linear correlation between device fill factor (*FF)* and *ISI* as depicted in **Figure 4a**. Similarly, the *FF* was also found to be correlated with the component scattering intensity (*CSI*) of the high-*q* peak as shown in **Figure 4b**, where *CSI* describes the relative average composition variation of the two different length scales. Higher values indicate higher purity, which is beneficial for reducing bimolecular recombination. Such purer domains provide a longer pathway for the charge transport and increase device performance.

Table 2. Inverted device performance of H11 and H12 based inverted OSC devices.

Device	J_{sc} *(mA/cm^2)*	V_{oc} *(V)*	*FF (%)*	*PCE (%)*
H11:IDIC As-cast	8.7 ± 0.3	1.00 ± 0.01	36.3 ± 0.60	3.15 ± 0.13
H11:IDIC Annealed	13.8 ± 0.3	0.97 ± 0.01	59.5 ± 1.06	7.98 ± 0.21

H12:IDIC As-cast	4.0 ± 0.2	0.89 ± 0.08	34.9 ± 1.37	1.25 ± 0.08
H12:IDIC Annealed	8.4 ± 0.4	0.87 ± 0.03	45.3 ± 0.45	3.30 ± 0.21

In this multi-length scale morphology, the length scale which contributes to charge dissociation at the donor-acceptor interface should mainly attribute to the smaller domains, as the long period of the smaller domains is comparable to typical exciton diffusion length of organic semiconductors. Thus, we see a clear correlation between the long period of the smaller domains and J_{sc}. Moreover, since the long period of the smaller domains is smaller for the H11-based blends (See **Figure 4c**), better exciton diffusion and hence higher charge generation rate are expected in this particular system. This is indeed consistent with the highest charge carrier generation rate being achieved in the H11 system from the current-voltage characteristics discussed in section 3.2. To have a deeper understanding of the role of morphology on photocurrent generation, J_{sc} is depicted against domain properties as shown in **Figures 4d-4f**. Specifically, the J_{sc} was found to be linearly decreasing with domain size (**Figure 4f**), which is an indicator of either less exciton dissociation in larger domains or poor charge carrier collection to electrodes. The H12-based system, which is identified by less pure and larger domain size, obviously suffers from smaller *FF,* lower generation rate and hence lower J_{sc}. As noted earlier, Flory-Huggins interaction parameters calculated from the solubility parameters for these two systems have shown that H11: IDIC blend has lower molecular miscibility. The estimated interaction parameter values are 2.52 and 2.35 for H11:IDIC and H12:IDIC systems respectively.[31] A higher value for the interaction parameter indicates lower miscibility hence higher purity. This observation clearly agrees with the domain purities obtained from R-SoXS.
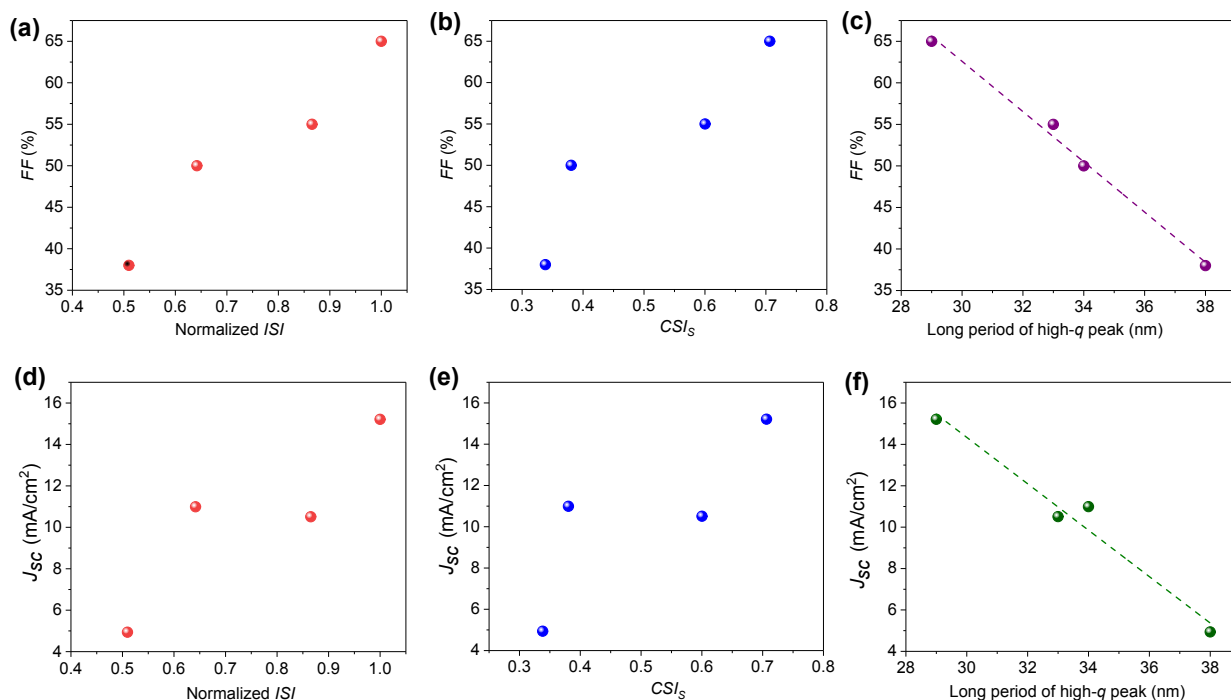
14

Figure 4 (a) Plot of Device *FF* as a function of normalized *ISI*; (b) Plot of Device *FF* as a function of component scattering intensity of high-*q* peak (CSI_S); (c) Plot of Device *FF* as a function of long period of high-*q* peak; (d) Plot of J_{sc} as a function of normalized *ISI;* (e) Plot of J_{sc} as a function of component scattering intensity of high-*q* peak (CSI_S); (f) Plot of J_{sc} as a function of long period of high-*q* peak. Dashed lines are linear fits to the raw data.

Achieving purer domains over annealing was further confirmed by photoluminescence (PL) measurements. The comparison of the as-cast blend and annealed blend PL spectra **(Figure S3)** shows a clear reduction in the flux in the as-cast samples compared to annealed ones. This can be explained as the excitons in the as-cast blends find an interface to dissociate immediately. On the other hand, the increase in the PL intensity in the annealed samples indicates that the singlet excitons are not splitting efficiently as it radiatively recombines at the pure phase. This confirms our finding in R-SoXS, domains get purer when annealed. It is also clear from the device parameters that annealing devices is critical to improving the device performance. This indicates

the importance of achieving more pure and smaller domains for improved device performance.

4. Conclusion

In this study, we applied R-SoXS to investigate the relationship between complex morphology and device performance in a pair of nonfullerene all-small molecule systems, which differs in the conjugation of side chains. A multi-length scale morphology was observed in the blends of H11 and H12 with IDIC, and the high-q long period, as well as the composition variations, correlates well with J_{sc} and *FF*. *FF* and J_{sc}, monotonically increase with *CSI* of the high-q domains and *ISI* while decreasing almost linearly with the high-q long period. Notably, this is the first report that shows such a strong correlation between device parameters and morphological parameters at the smaller length scale in nonfullerene all-small molecule OSCs. The ideality factor of the devices with H12 blend show higher deviation from unity and low α values at higher light intensities which are attributed to the inefficiencies in charge collection due to recombination. Higher domain purity and small domain sizes in H11 system reduce recombination and help charge dissociation respectively. Since the only difference between H11 and H12 is the conjugation of side chains, side chain modification of a small molecule can create a tremendous effect on device performance by altering the molecular interaction and multilength scale morphology. The system studied in this study is a clear example to show the result of side chain modification to improve device performance and the importance of the understanding of structure-functional relations for functional blends based on nonfullerene small molecules. We anticipate that developing *in-situ* R-SoXS will enable our understanding of the real-time evolution of complex morphology of this type of emerging solar cells.

Reference

1. S. Li, L. Ye, W. Zhao, H. Yan, B. Yang, D. Liu, W. Li, H. Ade and J. Hou, *J Am Chem Soc*, 2018, **140**, 7159-7167.
2. L. Meng, Y. Zhang, X. Wan, C. Li, X. Zhang, Y. Wang, X. Ke, Z. Xiao, L. Ding, R. Xia, H. L. Yip, Y. Cao and Y. Chen, *Science*, 2018, **361**, 1094-1098.
3. J. Q. Zhang, H. S. Tan, X. G. Guo, A. Facchetti and H. Yan, *Nature Energy*, 2018, **3**, 720-731.
4. C. Yan, S. Barlow, Z. Wang, H. Yan, A. K. Y. Jen, S. R. Marder and X. Zhan, *Nat. Rev. Mater.*, 2018, **3**, 18003.
5. C. Sun, F. Pan, H. Bin, J. Zhang, L. Xue, B. Qiu, Z. Wei, Z.-G. Zhang and Y. Li, *Nature Communications*, 2018, **9**, 743.
6. D. Deng, Y. Zhang, J. Zhang, Z. Wang, L. Zhu, J. Fang, B. Xia, Z. Wang, K. Lu, W. Ma and Z. Wei, *Nature Communications*, 2016, **7**, 13740.
7. J. E. Coughlin, Z. B. Henson, G. C. Welch and G. C. Bazan, *Accounts of Chemical Research*, 2014, **47**, 257-270.
8. C. Cui, X. Guo, J. Min, B. Guo, X. Cheng, M. Zhang, C. J. Brabec and Y. Li, *Advanced Materials*, 2015, **27**, 7469-7475.
9. B. Qiu, L. Xue, Y. Yang, H. Bin, Y. Zhang, C. Zhang, M. Xiao, K. Park, W. Morrison, Z.-G. Zhang and Y. Li, *Chemistry of Materials*, 2017, **29**, 7543-7553.
10. H. Li, Y. Zhao, J. Fang, X. Zhu, B. Xia, K. Lu, Z. Wang, J. Zhang, X. Guo and Z. Wei, *Advanced Energy Materials*, 2018, **8**, 1702377.
11. H. Bin, J. Yao, Y. Yang, I. Angunawela, C. Sun, L. Gao, L. Ye, B. Qiu, L. Xue, C. Zhu, C. Yang, Z.-G. Zhang, H. Ade and Y. Li, *Advanced Materials*, 2018, **30**, 1706361.
12. J. Guo, H. Bin, W. Wang, B. Chen, J. Guo, R. Sun, Z.-G. Zhang, X. Jiao, Y. Li and J. Min, *Journal of Materials Chemistry A*, 2018, **6**, 15675-15683.
13. M. Privado, P. de la Cruz, S. Biswas, R. Singhal, G. D. Sharma and F. Langa, *Journal of Materials Chemistry A*, 2018, **6**, 11714-11724.
14. L. Yang, S. Zhang, C. He, J. Zhang, Y. Yang, J. Zhu, Y. Cui, W. Zhao, H. Zhang, Y. Zhang, Z. Wei and J. Hou, *Chemistry of Materials*, 2018, **30**, 2129-2134.

15. Y. Wang, M. Chang, B. Kan, X. Wan, C. Li and Y. Chen, *ACS Applied Energy Materials*, 2018, **1**, 2150-2156.
16. N. Liang, D. Meng, Z. Ma, B. Kan, X. Meng, Z. Zheng, W. Jiang, Y. Li, X. Wan, J. Hou, W. Ma, Y. Chen and Z. Wang, *Advanced Energy Materials*, 2016, **7**, 1601664.
17. O. K. Kwon, J.-H. Park, D. W. Kim, S. K. Park and S. Y. Park, *Advanced Materials*, 2015, **27**, 1951-1956.
18. L. Yang, S. Zhang, C. He, J. Zhang, H. Yao, Y. Yang, Y. Zhang, W. Zhao and J. Hou, *Journal of the American Chemical Society*, 2017, **139**, 1958-1966.
19. Z. Zhou, S. Xu, J. Song, Y. Jin, Q. Yue, Y. Qian, F. Liu, F. Zhang and X. Zhu, *Nature Energy*, 2018.
20. J. Shi, A. Isakova, A. Abudulimu, M. van den Berg, O. K. Kwon, A. J. Meixner, S. Y. Park, D. Zhang, J. Gierschner and L. Lüer, *Energy & Environmental Science*, 2018, **11**, 211-220.
21. J. Hong, M. J. Sung, H. Cha, C. E. Park, J. R. Durrant, T. K. An, Y.-H. Kim and S.-K. Kwon, *ACS Applied Materials & Interfaces*, 2018.
22. G. Han and Y. Yi, *Advanced Theory and Simulations*, 2018, **0**, 1800091.
23. G. Long, B. Wu, A. Solanki, X. Yang, B. Kan, X. Liu, D. Wu, Z. Xu, W.-R. Wu, U. S. Jeng, J. Lin, M. Li, Y. Wang, X. Wan, T. C. Sum and Y. Chen, *Advanced Energy Materials*, 2016, **6**, 1600961.
24. O. Alqahtani, M. Babics, J. Gorenflot, V. Savikhin, T. Ferron, A. Balawi, A. Paulke, Z. Kan, M. Pope, A. J. Clulow, J. Wolf, P. L. Burn, G. Ian, N. Dieter, M. F. Toney, F. Laquai, P. M. Beaujuge and B. A. Collins, *Adv. Energy Mater.*, 2018, **8**, 1702941.
25. J. Min, X. C. Jiao, I. Ata, A. Osvet, T. Ameri, P. Bauerle, H. Ade and C. J. Brabec, *Advanced Energy Materials*, 2016, **6**, 1502579.
26. K. Gao, J. Miao, L. Xiao, W. Deng, Y. Kan, T. Liang, C. Wang, F. Huang, J. Peng, Y. Cao, F. Liu, T. P. Russell, H. Wu and X. Peng, *Advanced Materials*, 2016, **28**, 4727-4733.
27. C. He and J. Hou, *Acta Phys. -Chim. Sin.*, 2018, **34**, 1202-1210.
28. Y. Li, *Accounts of Chemical Research*, 2012, **45**, 723-733.
29. L. Ye, S. Zhang, L. Huo, M. Zhang and J. Hou, *Accounts of Chemical Research*, 2014, **47**, 1595-1603.
30. Y. Chen, X. Wan and G. Long, *Accounts of Chemical Research*, 2013, **46**, 2645-2655.
31. H. Bin, Y. Yang, Z. G. Zhang, L. Ye, M. Ghasemi, S. Chen, Y. Zhang, C. Zhang, C. Sun, L. Xue, C. Yang, H. Ade and Y. Li, *J. Am. Chem. Soc.*, 2017, **139**, 5085-5094.
32. X. Jiao, L. Ye and H. Ade, *Adv. Energy Mater.* , 2017, **7**, 1700084.
33. E. Gann, A. T. Young, B. A. Collins, H. Yan, J. Nasiatka, H. A. Padmore, H. Ade, A. Hexemer and C. Wang, *Rev. Sci. Instrum.*, 2012, **83**, 045110.
34. F. Liu, M. A. Brady and C. Wang, *European Polymer Journal*, 2016, **81**, 555-568.
35. J. Ilavsky, *Journal of Applied Crystallography*, 2012, **45**, 324-328.
36. L. Ye, B. A. Collins, X. Jiao, J. Zhao, H. Yan and H. Ade, *Adv. Energy Mater.*, 2018, **8**, 1703058.
37. L. Ye, H. Hu, M. Ghasemi, T. Wang, B. A. Collins, J.-H. Kim, K. Jiang, J. H. Carpenter, H. Li, Z. Li, T. McAfee, J. Zhao, X. Chen, J. L. Y. Lai, T. Ma, J.-L. Bredas, H. Yan and H. Ade, *Nature Materials*, 2018, **17**, 253-260.
38. J. H. Carpenter, A. Hunt and H. Ade, *J. Electron. Spectrosc. Relat. Phenom.*, 2015, **200**, 2-14.
39. F. Cser, *Journal of Applied Polymer Science*, 2001, **80**, 2300-2308.

40. L. Ye, Y. Xiong, S. Li, M. Ghasemi, N. Balar, J. Turner, A. Gadisa, J. Hou, B. T. O'Connor and H. Ade, *Adv. Funct. Mater.*, 2017, **27**, 1702016.
41. E. Limpert, W. A. Stahel and M. Abbt, *BioScience*, 2001, **51**, 341-352.
42. S. Mukherjee, X. Jiao and H. Ade, *Adv. Energy Mater.*, 2016, **6**, 1600699.
43. L. Ye, Y. Xiong, H. Yao, A. Gadisa, H. Zhang, S. Li, M. Ghasemi, N. Balar, A. Hunt, B. T. O'Connor, J. Hou and H. Ade, *Chem. Mater.*, 2016, **28**, 7451-7458.
44. V. D. Mihailetchi, J. Wildeman and P. W. M. Blom, *Physical Review Letters*, 2005, **94**, 126602.
45. R. Sokel and R. C. Hughes, *Journal of Applied Physics*, 1982, **53**, 7414-7424.
46. S. R. Cowan, A. Roy and A. J. Heeger, *Physical Review B*, 2010, **82**, 245207.
47. A. C. Stuart, J. R. Tumbleston, H. Zhou, W. Li, S. Liu, H. Ade and W. You, *Journal of the American Chemical Society*, 2013, **135**, 1806-1815.
48. X. Y. Liu, L. Ye, W. C. Zhao, S. Q. Zhang, S. S. Li, G. M. Su, C. Wang, H. Ade and J. H. Hou, *Materials Chemistry Frontiers*, 2017, **1**, 2057-2064.